



# Laser-induced ultrasonic imaging for measurements of solid surfaces in optically opaque liquids [Invited]

VASILY ZARUBIN,<sup>1,2,\*</sup> ANTON BYCHKOV,<sup>1,2</sup> ALEXANDER KARABUTOV,<sup>1,3,4</sup> VARVARA SIMONOVA,<sup>4</sup> AND ELENA CHEREPETSKAYA<sup>1</sup>

<sup>1</sup>Moscow Mining Institute, The National University of Science and Technology MISiS, 6 Leninskiy prospect, Moscow 119991, Russia

<sup>2</sup>Faculty of Physics, M.V. Lomonosov Moscow State University, 1 Leninskiye Gory, Moscow 119991, Russia

<sup>3</sup>International Laser Center, M.V. Lomonosov Moscow State University, 1 Leninskiye Gory, Moscow 119991, Russia

<sup>4</sup>The Institute on Laser and Information Technologies of the Russian Academy of Sciences, 1 Svyatozerskaya st., 140700 Shatura, Moscow Region, Russia

\*Corresponding author: zarubin.vasily@gmail.com

Received 3 November 2017; revised 22 January 2018; accepted 22 January 2018; posted 23 January 2018 (Doc. ID 312633); published 16 February 2018

The paper describes a novel laser ultrasonic profilometry method which uses pulsed laser radiation for imaging of the surface profile of solid objects in optically opaque liquids by scattering of ultrasonic waves. Algorithms for the construction of laser ultrasonic images and for profile segmentation are presented. An experimental setup for profile measurements is described. It allows reconstructing of laser ultrasonic images with a frame rate of 10 Hz and performing an automated 3D scanning of samples. The results of the experimental testing of laser ultrasonic profilometry on duralumin samples are presented. The approximation error of duralumin cylinder surface profile measurements in water is 15  $\mu\text{m}$ . The results are compared to those obtained by x-ray tomography. © 2018 Optical Society of America

**OCIS codes:** (110.5125) Photoacoustics; (110.7170) Ultrasound; (120.6660) Surface measurements, roughness; (170.0110) Imaging systems; (100.0100) Image processing.

<https://doi.org/10.1364/AO.57.000C70>

## 1. INTRODUCTION

The problem of surface profile measurements is important for a wide range of industrial control applications. On the one hand, profilometry is used for a set of applications that does not require high spatial resolution, but the control area is large [1]. These applications include detection of the critical cracks and defects on the surfaces of pipes and reservoirs. On the other hand, there are problems that require very high resolution, while the control area is small. Such problems include a control of polymeric films with embossed surfaces [2], parts for high precision and optical systems [3,4], and others. Generally, profilometry is conducted using methods that could be divided into two groups—contact and non-contact.

The typical method of contact profilometry is a method of mechanical stylus profilometry [5,6]. Despite the relative simplicity of the device design, profilometers of this type reliably provide high-resolution measurements of the solids profile with a wide range of measurement ranges. The difficulties in operating with the sensitive films, a need for preliminary preparation of samples, and a poor scan speed are among the drawbacks of contact profilometers.

The problems mentioned above can be solved by using non-contact profilometry methods—optical and ultrasonic. The most commonly used methods of optical profilometry are laser interferometry and laser triangulation [7–9]. Their advantages include high resolution, comparable with that provided by stylus profilometers. However, a raster scanning technique results in a low speed of operation for these methods. Currently, different types of a fringe-projection phase-shift profilometry method are being developed to implement a real-time mapping of the surfaces [10–15]. Their advantages are a high frame rate, which reaches 40 Hz, and a relatively simple device design. But high-precision optical profilometry requires expensive preliminary washing of samples, which is often incompatible with the requirements of industrial control. Besides, optical methods cannot be used for control of the contaminated objects in opaque liquids, such as oil pipes, tanks, and objects with optically absorbing surfaces. Therefore, it is reasonable to use ultrasonic methods for a number of industrial problems.

The most appropriate ultrasonic method for conduction of profile measurements is acoustical microscopy [16,17]. It uses a high-frequency (over 50 MHz) ultrasound, which provides up

to submicrometer resolution and raster scanning. However, high frequencies are strongly attenuated in organic liquids (e.g., oil). This limits the resolution of ultrasonic profilometry to 10 μm. Nevertheless, such resolution is sufficient for many applications.

Current investigation uses one of the photoacoustic methods, called laser ultrasound tomography [18], for the high-speed profilometry of objects in liquids. This approach has a number of advantages over traditional methods of the sample profile imaging and allows using optical radiation for imaging of the samples in optically opaque liquids.

## 2. BASICS OF LASER ULTRASONIC PROFILOMETRY

Laser ultrasonic profilometry is based on optoacoustic effect [19], and the primary mechanism is thermoelastic expansion. Figure 1(a) presents the schematics of laser ultrasonic profilometry setup. Pulsed laser light is used to generate the short ultrasonic probing pulse [Fig. 1(b)] by the near-surface optical absorption of the laser beam in the dedicated optoacoustic generator—a plane-parallel polymeric absorbing medium. The optical absorption leads to the local heating of the medium with corresponding temperature rise and its subsequent nonstationary expansion. The rapid expansion leads to the generation of broadband ultrasonic waves.

The general equations for the acoustic velocity potentials describing the thermal excitation of the ultrasound in isotropic solid heat conducting medium can be written in the following form:

$$\begin{cases} \frac{1}{c_L^2} \frac{\partial^2 \phi}{\partial t^2} - \Delta \phi = -\beta \left( 1 - 4 \frac{c_T^2}{3c_L^2} \right) \frac{\partial T}{\partial t}, \\ \frac{1}{c_T^2} \frac{\partial^2 \psi}{\partial t^2} - \Delta \psi = 0, \\ \frac{\partial T}{\partial t} = \chi \Delta T - \frac{(\nabla \cdot \langle S \rangle)}{\rho_0 c_p}. \end{cases} \quad (1)$$

Here,  $\phi, \psi$  are scalar and vector acoustic velocity potentials, respectively;  $\mathbf{v} = \nabla \phi + (\nabla \times \psi)$  is acoustic particle velocity;  $\chi$  is thermal diffusivity coefficient;  $c_L, c_T$  are the speed of longitudinal and transverse bulk acoustic waves, respectively;  $\beta$  is thermal expansion coefficient;  $T$  is perturbation of temperature; and  $\langle S \rangle$  is the Poynting vector of the incident electromagnetic wave. As it follows from Eq. (1), the infinite solid medium generates only scalar velocity field, corresponding to

longitudinal bulk waves, under heat impact. Its solenoidal component (transverse waves) can be generated only when the beam is reflected on the border of medium.

The polymeric material of the optoacoustic generator has a very low thermal diffusivity coefficient, so heat conduction can be neglected. The intensity of the laser beam in the optoacoustic generator can be found with Beer's law:  $I(x, y, z, t) = I_0(x, y)e^{-\alpha(x-z_g)}f(t)$ , where  $\alpha$  is the optical absorption coefficient, and  $z_g$  is the position of the optoacoustic generator. Since  $|\partial I/\partial x|, |\partial I/\partial y| \ll \alpha I$ , gradients in  $x$  and  $y$  directions can be neglected along with transverse acoustic waves:

$$\frac{1}{c_L^2} \frac{\partial^2 \phi}{\partial t^2} - \Delta \phi = -\frac{\alpha \beta}{\rho_0 c_p} \left( 1 - 4 \frac{c_T^2}{3c_L^2} \right) I(x, y, z, t). \quad (2)$$

The generated probing ultrasonic pulse is focused by the acoustic lens, and then it propagates through the immersion liquid and is partially reflected from the surface of the sample. The array of detectors is used to record the reflected back waves as electric signals. Then the signals are processed to reconstruct an image of the sample surface. The multi-detector approach significantly increases the speed of profilometry compared to the traditional ultrasonic raster scanning and allows inspection of samples of more complex shapes.

The advantage of the laser method of ultrasound generation is a possibility to generate high-power short aperiodic pulses, which are unreachable for other ultrasonic generators [Fig. 1(b)] [20]. A short duration of the probe pulse with a high ratio of the upper-to-lower cutoff frequencies leads to an increase of the longitudinal spatial resolution compared to the common methods of ultrasound generation. Another advantage of the laser ultrasound source is the absence of the sidelobes in the directivity pattern due to the smooth wavefront  $I_0(x, y)$  of the laser beam.

## 3. EXPERIMENTAL SETUP

The experimental setup is presented in Fig. 2 [21]. Optical radiation of a Q-switched Nd:YAG laser (wavelength  $\lambda = 1064$  nm, pulse duration  $\tau = 10$  ns, pulse rate 20 Hz) is delivered by a multimode silica fiber (NA = 0.22) to an optoacoustic generator for laser excitation of ultrasonic pulse. The optical beam is spread on the flat surface of the generator by a system of lenses. A flat-concave acoustical lens focuses the laser ultrasonic probing pulse on the sample. It passes through immersion liquid (water), partially reflects from the surface of the sample under inspection, and passes backwards through the same lens to be recorded by a plane piezoelectric detector array of 16 polyvinylidene fluoride transducers (length, 20 mm; width, 1 mm; gap between transducers, 1 mm). Detector array provides effective reception of ultrasound in the frequency band of 1.6–9 MHz [22]. Although the transducers are flat, they are glued to the flat surface of the acoustic lens. This makes the array effectively cylindrical (focal distance, 40.1 mm). To obtain a high-resolution tomogram, the sample has to be moved to the array focus by the three translational axes of the four-coordinate positioning system. The fourth axis is rotational, and it is designed for 3D step-by-step scanning of the samples.

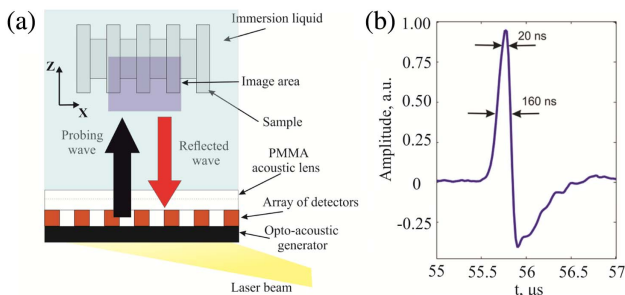


**Fig. 1.** (a) Principle of laser ultrasonic profilometry. (b) Experimentally recorded laser ultrasonic probing pulse, which was reflected from the duralumin plane-parallel plate (acoustic reflector).

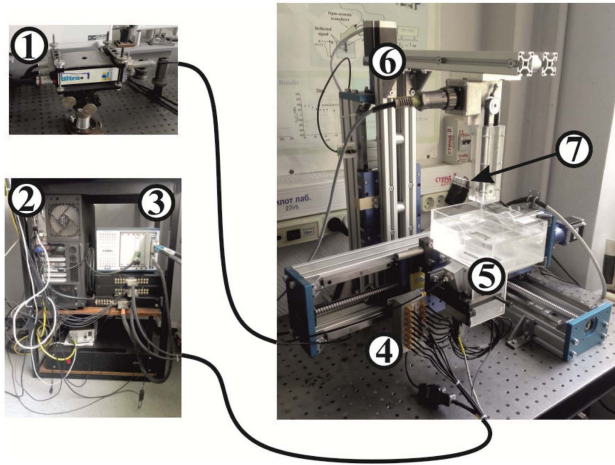


**Fig. 2.** Experimental setup. 1, Nd:YAG laser head; 2, personal computer with GPU; 3, high-speed data acquisition and data-processing system; 4, multichannel preamplifier; 5, wideband laser ultrasonic module (opto-acoustic generator and acoustical antenna); 6, four-axis positioning system; 7, solid sample.

The analog electrical signals from the piezoelectric transducers after pre-amplifier are received by a high-speed multichannel data acquisition and processing system (NI FlexRIO 5752). It digitizes signals using a 50 MHz multichannel analog-to-digital converter (ADC). The Field Programmable Gate Array (FPGA) acquires digital data, averages and transfers digital data to a personal computer for further real-time data processing, and handles the construction of laser ultrasonic images and segmentation of the surface profile.

A specialized software with a graphical user interface was developed to operate the experimental setup. It displays images of acoustic inhomogeneities (including the solid sample–immersion liquid boundary) in the focal plane of the detector array in real time with a frame rate of 10 Hz. The filtered back-projections algorithm is used for construction of laser ultrasonic images [23]. The profile of the sample is segmented on an image by specially developed image-processing algorithms. They are parallelized using NVIDIA CUDA [24] on graphical processing units (NVIDIA GeForce GTX 770) and with use of computer vision library OpenCV.

## 4. ALGORITHMS

### A. Reconstruction of Laser Ultrasonic Images

The back-projection algorithm constructs an image over “arcs of probability,” which have parabolic shape. Suppose the acoustic inhomogeneity (e.g., the element of the sample surface) is located in the point  $\mathbf{r} = (x, z)$  of the image plane. The plane-wave probing ultrasonic pulse first propagates in the immersion liquid from  $z_g$  to  $z$ , is then scattered by the inhomogeneity, and finally propagates from the inhomogeneity to the  $i$ th receiver at the point  $\mathbf{d}_i = (x_i, z_i)$ . The total travel time of the pulse is  $t_i = (z - z_g + |\mathbf{d}_i - \mathbf{r}|)/c$ , where  $c$  is the speed of sound in the immersion liquid. So, the effective amplitude of acoustical inhomogeneities  $\epsilon(\mathbf{r})$  (values of the image pixels) in point  $\mathbf{r}$  is given by a formula [23]

$$\epsilon(\mathbf{r}) = \frac{\sum_{i=1}^N \Delta\Omega_i \cdot b(\mathbf{d}_i, t = \frac{z - z_g + |\mathbf{d}_i - \mathbf{r}|}{c})}{\sum_{i=1}^N \Delta\Omega_i}, \quad (3)$$

where  $N$  is the number of transducers, and  $\Delta\Omega_i$  is a solid angle that subtends the  $i$ th transducer as it is seen from point  $\mathbf{r}$ . A solid angle is introduced to take into account the rate of acoustic energies received by different transducers. Value of a back-projection  $b(\mathbf{d}_i, t)$  is calculated with the following formula:

$$b(\mathbf{d}_i, t) = -\frac{\partial p(\mathbf{d}_i, t)}{\partial t}, \quad (4)$$

where  $p(\mathbf{d}_i, t)$  is a pressure signal, detected by the  $i$ th transducer. The pressure signals are filtered by a pass-band filter:

$$K(f) = K_0 \exp\left(-\left(\frac{f_l}{f}\right)^8 - \left(\frac{f_l}{f}\right)^2 - \left(\frac{f}{f_b}\right)^4\right), \quad (5)$$

where  $f_l = 0.5$  MHz,  $f_b = 10$  MHz are lower and upper spectrum cutoff frequencies, respectively, determined by the frequency band of the polyvinylidene fluoride transducers and by a noise spectrum of the experimental setup. According to the theory of sound scattering [25], waves with a wavelength  $\lambda \sim 2a$  are effectively scattered by a single inhomogeneity of size  $a$ . Thus, the laser ultrasonic imaging system can effectively image single acoustic scatterers with a size down to 150  $\mu\text{m}$ . Higher precision can be achieved using *a priori* information about the sample and statistical processing of the results.

We have reconstructed laser ultrasonic images and profiles of the three sample solid objects made of duralumin (D16T) to test the experimental setup and the developed technique. These samples are shown in Fig. 2: a cylinder (diameter, 14 mm; length, 38 mm), a cylinder with irregular grooves (diameter, 14 mm; length, 38 mm; depth of grooves, 2 mm; width of grooves, 2 mm), a cylinder with irregular grooves (diameter, 14 mm; length, 38 mm; depth of grooves, 1 mm; width of grooves, 2 mm–6 mm). The outer surface profiles of the sample objects are clearly visible on the reconstructed laser ultrasonic images (on the left of Fig. 3).

### B. 2D Profile Reconstruction

The acoustic impedance of the solid object  $Z_1 = \rho_1 c_1$ , where  $\rho_1$  is the density of the object and  $c_1$  is the speed of sound in the object, is usually much greater than the acoustic impedance of the immersion liquid  $Z = \rho c$ , so the reflection coefficient for pressure  $R = (Z_1 - Z)/(Z_1 + Z)$ . Thus, the probing ultrasonic pressure pulse retains the sign upon reflection. Therefore, in the laser ultrasonic images  $\epsilon(x, z)$ , the boundaries of a solid object are positive peaks ( $\epsilon(x, z) > 0$ ). The sizes of such peaks along the  $z$  axis correspond to the length of the ultrasonic probe pulse in the immersion liquid. This allows us to give a rigorous definition of the surface profile of a solid object in the method of laser ultrasonic profilometry.

Let  $M$  be a set of points  $(x, z)$  on the laser ultrasonic image  $\epsilon(x, z)$  in which this function has a local maximum along the  $z$  axis:

$$M = \left\{ (x, z): \left(\frac{\partial \epsilon}{\partial z}\right)_{(x,z)} = 0, \left(\frac{\partial^2 \epsilon}{\partial z^2}\right)_{(x,z)} < 0 \right\}. \quad (6)$$

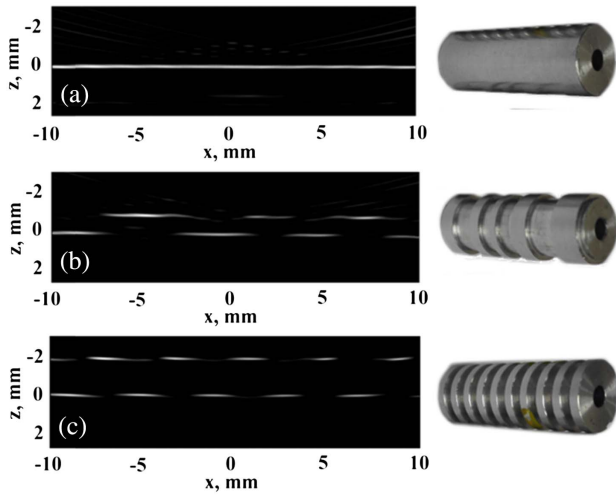


**Fig. 3.** Laser ultrasonic images  $\epsilon(x, z)$  of the duralumin samples reconstructed using filtered back-projection algorithm: (a) a cylinder 14 mm in diameter, (b) a cylinder 14 mm in diameter with irregular grooves 1 mm in depth, and (c) a cylinder 14 mm in diameter with regular grooves 2 mm in depth.

The outer surface profile of the sample, reconstructed from the laser ultrasonic images  $\epsilon(x, z)$ , will be the subset of  $M$  closest to the receiving detector array along the  $z$  axis (the axis is directed to the detector array in Fig. 3):

$$z_p(x) = \max_z M. \quad (7)$$

In other words, the outer surface profile is the line of local maxima closest to the detector array.

The high sampling frequency of the ADC  $f_d = 50 \text{ MHz} > 2f_b = 20 \text{ MHz}$  allows reconstructing of laser ultrasonic images with pixel sizes  $dz \sim 10 \text{ } \mu\text{m} \ll c/f_b = 150 \text{ } \mu\text{m}$  by interpolation of digitized ultrasonic signals between samples. The sampling theorem can again be used to interpolate the laser ultrasonic image  $\epsilon(x, z)$  along the  $z$  axis to improve accuracy of the reconstructed profile. First for each  $x$ , an approximate position of the maximum closest to the detector array is determined. Then a quadratic interpolation of the function  $\epsilon(x, z)$  is carried out in the vicinity of the approximate maximum to get the refined position  $z_p(x)$  of the maximum. Figure 3(a) shows the laser ultrasonic image of a duralumin cylinder submerged in water, and Fig. 4(a) shows the reconstructed profile  $z_p(x)$ .

If it is *a priori* known that the surface profile consists of straight-line segments, it is possible to improve the accuracy of profile reconstruction and to evaluate the deviations of the surface profile from the approximate line. The Hough transform [26] (a computer vision method conceptually close to the Radon transform) is used to determine the number and approximate position of the line segments in the image  $\epsilon(x, z)$ .

Any straight line in the image space  $(x, z)$   $\rho = x \cos \theta + z \sin \theta$  can be represented as a single point  $(\rho, \theta)$  in the parameter space, where  $\rho$  is the distance from the line to the upper left corner of the image, and  $\theta$  is the angle between the line and the  $z$  axis [Fig. 4(a)]. A set of all possible lines going

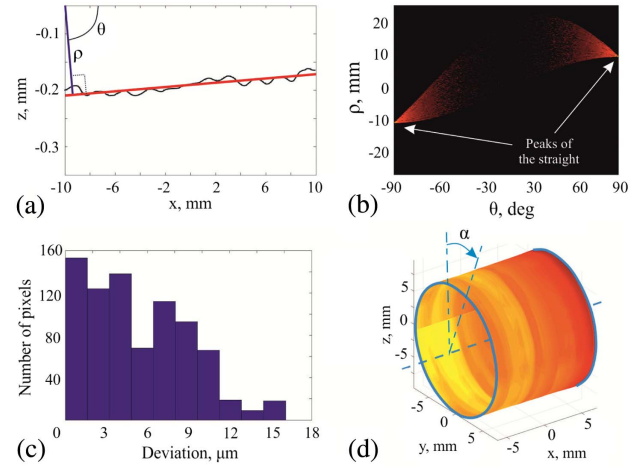


**Fig. 4.** Processing of the cylinder tomogram: (a) line of tomogram maxima, (b) the Hough diagram  $A(\rho, \theta)$ , (c) histogram of deviations of profile  $z_p(x)$  from the approximated line  $z_a(x)$ , (d) 3D map of the surface  $p(x, \alpha)$ .

through a single point in the image space  $(x, z)$  corresponds to a sinusoidal curve in the parameter space  $(\rho, \theta)$ .

First, the image is binarized  $\epsilon(x, z) \rightarrow \epsilon_b(x, z)$ : all values above a globally determined threshold are replaced with ones, and all the others with zeros. Then the distribution  $A(\rho, \theta)$  is calculated: each non-zero pixel of the binary image  $\epsilon_b(x, z)$  adds a sinusoidal curve to the image  $A(\rho, \theta)$ . If there is a single straight line with parameters  $(\rho, \theta)$  in the image  $\epsilon_b(x, z)$ , then all the sinusoidal curves will intersect in two points:  $(\rho, \theta)$  and  $(-\rho, \theta + \pi)$ . Thus,  $A(\rho, \theta)$  characterizes the probability of existence of a straight line with parameters  $(\rho, \theta)$  in the image  $\epsilon_b(x, z)$ . Figure 4(b) shows the distribution  $A(\rho, \theta)$ , which corresponds to the laser ultrasonic image in Fig. 4(a). Two bright peaks ( $|\rho| \approx 10 \text{ mm}$ ,  $|\theta| \approx 90^\circ$ ) in Fig. 4(b) are intersection points of the multiple sinusoidal curves.

The distribution  $A(\rho, \theta)$  allows determining the number and parameters of straight line segments in the laser ultrasonic image. We used the linear least-squares method to approximate the profile and to determine the approximation errors:

$$\begin{cases} z_a(x) = kx + b, \\ \int (z_p(x) - z_a(x))^2 dx \rightarrow \min. \end{cases} \quad (8)$$

Equation (8) makes it possible to quantify the accuracy of the profile measurements by plotting the histogram of the deviations of the profile points  $|z_p - z_a|$  from the approximating straight line  $z_a(x)$ . Figure 4(c) shows the histogram for the duralumin cylinder: for 95% of all points, the deviation is less than  $15 \text{ } \mu\text{m}$ . Thus, the outer surface profile can be reconstructed with high accuracy using the developed techniques and experimental setup.

### C. 3D Surface Map Reconstruction

A 3D surface map  $(x, \alpha)$  of the sample is reconstructed by rotating the sample in steps of  $\Delta\alpha$  and constructing a surface profile  $z_p(x)$  for each angle  $\alpha$ . Here  $\alpha$  is the angular coordinate of the rotational axis. Figure 4(d) shows the 3D surface map  $p(x, \alpha)$  of a duralumin cylinder, and the deviations from the

ideal cylindrical surface are color-coded: yellow means closer to the axis of the cylinder, and red means farther from the axis of the cylinder.

The optimal angular step  $\Delta\alpha$  is determined by the width of the sensitivity region of the detector array in a direction perpendicular to the image plane:  $\Delta y = 0.4$  mm, and by the radius of the sample object  $R \sim 10$  mm:  $\Delta\alpha < \Delta y/R \approx 2.3^\circ$ .

The rotational axis has to be parallel to the detector array plane and be in its focal plane to construct correct 3D maps of the surface. A simple image correction procedure is performed to decrease the impact of any misalignment. The rotational axis itself was scanned step-by-step (full turn) without any sample. An equation defining the axis position was calculated on each step. All data from subsequent experiments were corrected by means of these results.

The average diameter of the cylinder (13.94 mm in diameter), which was measured by the map  $p(x, \alpha)$ , is 14.26 mm. The differences are mainly due to the aforementioned misalignment, which could not be fully compensated by the simple correction procedure, and more advanced techniques have to be applied.

## 5. RESULTS AND DISCUSSION

Laser ultrasonic profile measurements were compared to those obtained by the x-ray tomograph (Nordson XD7600NT) (Fig. 5).

The depth of grooves measured by the laser ultrasonic tomography is denoted by  $h_{lu}$ , and the depth measured by the x-ray tomography is denoted by  $h_{xr}$ . Both methods provide similar results as it follows from the data table: grooves depth for the cylinder with regular grooves is

$$h_{xr} = (1.968 \pm 0.005) \text{ mm},$$

$$h_{lu} = (1.972 \pm 0.005) \text{ mm},$$

and grooves depth for the cylinder with irregular grooves is

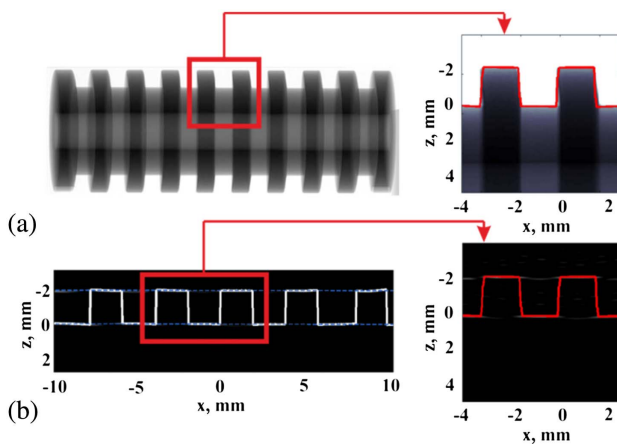


**Fig. 5.** Cylinder with regular grooves (depth and width 2 mm): (a) x-ray image superposed with segmented profile, measured by laser ultrasonic method; (b) laser ultrasonic image with segmented profile and grooves boundaries on it.

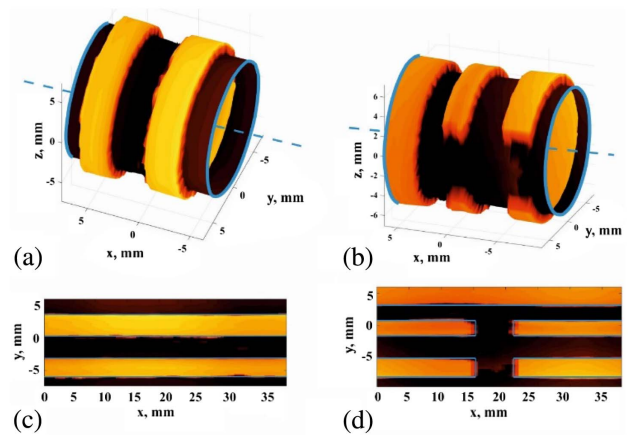


**Fig. 6.** (a), (c) Images of the cylinder with irregular grooves. (b), (d) Images of the cylinder with irregular grooves and slots. (a), (b) Reconstructed 3D images of cylinder surface. (c), (d) 2D projections of the corresponding 3D maps. Bright color denotes more distant parts from the center of the sample, and dark color denotes closer parts to the center. The blue lines are auxiliary, denoting the boundaries of the relief.

$$h_{xr} = (0.959 \pm 0.005) \text{ mm},$$

$$h_{lu} = (0.988 \pm 0.004) \text{ mm}.$$

Figure 6(a) shows a 3D map of the surface of the cylinder with irregular grooves, and Fig. 6(b) shows a 3D map of the same sample, but with two slots in the grooves. Each slot has a depth of 1 mm and a length of 6.9 mm in tangential direction. An average groove depth measured by the x-ray tomograph (0.959 mm) is close to that measured with the laser ultrasonic 3D surface map (0.935 mm). The measured width of groove is 3.34 mm, and it differs from the real width of 3.06 mm. The measured length of slots is 6.4 mm; it matches their real length within the transversal resolution  $\Delta y = 0.4$  mm. The diameter of the outer boundary measured by laser ultrasonic method (14.01 mm) is similar to its real diameter (14.14 mm). As it is seen from the results, the accuracy of the relative measurements (depth of grooves) is higher than the accuracy of the absolute measurements (diameter of grooves). This is due to the aforementioned difficulties with the misalignment elimination.

One of the drawbacks of all ultrasonic methods is the relatively low transverse resolution, which is caused by the integration of the acoustic signal over the surface of the transducers. This leads to the distortions of the vertical boundaries in Figs. 6(c) and 6(d). The size of such distortions is 150–300  $\mu\text{m}$ . The transverse spatial resolution can be improved by using detector arrays with smaller detector widths or by using a confocal toroidal array [27].

Acoustic and geometric properties of the samples, acoustic path properties, and axes misalignments determine the resolution of the laser ultrasound profilometry [22,27]. Dispersion and attenuation of the ultrasound travelling through the immersion liquid and detector array are negligible. One of the key factors is the temperature stability: the change of the water temperature by  $1^\circ\text{C}$  leads to a change of speed of sound by

3 m/s [28] and to the 4  $\mu\text{m}$  error of groove-depth measurement (with 2 mm depth). However, this problem can be solved by additional measurements of ultrasound velocity using reference surfaces.

According to the algorithms used, the position of the vertical boundary is determined by the edgepoint of the groove. Scattering of a probing pulse plane wave at the edge generates a circular wave. Therefore, a groove edge acts as a point acoustic scatterer. Hence the transverse resolution is actually determined by the width of the point-spread function [27]. The experimental accuracy of determination of the position of the vertical boundaries was 150–300  $\mu\text{m}$ .

The resolution of the experimental setup decreases if the inspected sample surface is inclined in the  $x$ - $z$  plane: wave vectors are shifted from the area of maximal sensitivity of transducers, and the received signal is integrated over time. The limitation for the experimental setup used in current work is  $|\theta - 90^\circ| < 10^\circ$ .

## 6. CONCLUSION

The laser ultrasonic profile evaluation technique and the experimental setup are presented. They use pulsed laser light to generate ultrasound for imaging of the profile of solids immersed in liquids, which can be optically opaque. The prototype of the four-axis automated laser ultrasonic profilometer operating in real time (frame rate is up to 10 Hz) is designed and tested. The method and parallel algorithms for imaging of 3D profile of solids of revolution are developed. The parameters of the cylindrical samples with grooves were measured using the experimental setup. These results were compared to those obtained by x-ray tomography. The comparison shows the accordance of grooves-depth measurements in the longitudinal direction within 15  $\mu\text{m}$ . However, the error of measurements of transverse sizes of grooves is 150–300  $\mu\text{m}$ . The accuracy can be improved by optimization of the detector array geometry of the specific samples. The diameters of the cylinders measured by means of the 3D laser ultrasonic profile maps differ from that measured by a caliper by the value of 100  $\mu\text{m}$ . The error is caused mainly by the complexity of the technical sample alignment.

The obtained results show that laser ultrasound profilometry is a promising method for imaging of the macroscopic surface profile of solid objects in optically opaque liquids. This makes it possible to measure thickness, depth, and height with a resolution of up to dozens of micrometers. Furthermore, the task of laser-ultrasound profilometry with relatively high resolution is one of the important steps toward the development of the method of laser ultrasonic tomography of bodies with non-planar surface. The ability to determine body surface profile is a key step in the tomographic algorithms that take into account the refraction of the ultrasonic beam at the solid-liquid boundary. Thus, laser ultrasonic profilometry enables the development of a method of laser ultrasonic structuroscopy and defectoscopy of solids with non-planar surfaces.

**Funding.** NUST “MISiS” Competitiveness Program by the Ministry of Education and Science of the Russian Federation

(Minobrnauka) (K2-2017-003); Russian Science Foundation (RSF) (16-17-10181).

**Acknowledgment.** This paper is based on the talk presented at the 13th School on Acousto-Optics and Applications, Moscow, Russia, June 19–23, 2017. V. P. Zarubin, A. S. Bychkov, V. A. Simonova, A. A. Karabutov, and E. B. Cherepetskaya, “3D measurement of solid surface using laser ultrasound tomography,” *Program and Abstracts Book*, p. 56.

## REFERENCES

1. L. C. Lynnworth, *Ultrasonic Measurements for Process Control: Theory, Techniques, Application* (Academic, 2013).
2. L. de Haan, V. Gimenez-Pinto, A. Konya, T. Nguyen, J. Verjans, C. Sanchez-Somolinos, J. Selinger, R. L. Selinger, D. Broer, and A. Schenning, “Accordion-like actuators of multiple 3D patterned liquid crystal polymer films,” *Adv. Funct. Mater.* **24**, 1251–1258 (2014).
3. B. H. Lu, J. L. Zhang, B. G. Liu, Y. H. Sun, and G. D. Liu, “Laser interfering profilometer for micro-ball whole surface measurement,” *Proc. SPIE* **9142**, 91420A (2014).
4. M. Inam, V. Srivastava, and D. S. Mehta, “Three-dimensional profilometry of microlenses by phase shifting interferometry using nematic liquid crystal material filled cell as a phase modulator,” *Appl. Opt.* **54**, 1085–1089 (2015).
5. J. M. Alves, M. C. Brito, J. M. Serra, and A. M. Valleria, “A differential mechanical profilometer for thickness measurement,” *Rev. Sci. Instrum.* **75**, 5362–5363 (2004).
6. D. H. Lee and N. G. Cho, “Assessment of surface profile data acquired by a stylus profilometer,” *Meas. Sci. Technol.* **23**, 105601 (2013).
7. M. F. Costa, “Dimensional inspection of rough surfaces by optical triangulation,” *J. Indian Inst. Sci.* **76**, 279–287 (1996).
8. J. Schmit, J. Reed, R. Novak, and J. K. Gimzewski, “Performance advances in interferometric optical profilers for imaging and testing,” *J. Opt. A* **10**, 064001 (2008).
9. P. Vangla and G. M. Latha, “Surface topological analysis of geomembranes and sand using a 3D optical profilometer,” *Geosynth. Int.* **24**, 151–166 (2016).
10. S. Van der Jeught, J. A. Soons, and J. J. Dirckx, “Real-time microscopic phase-shifting profilometry,” *Appl. Opt.* **54**, 4953–4959 (2015).
11. B. Li, Y. An, and S. Zhang, “Single-shot absolute 3D shape measurement with Fourier transform profilometry,” *Appl. Opt.* **55**, 5219–5225 (2016).
12. G. Kösoğlu, H. Yüksel, and M. N. Inci, “Phase stepping optical profilometry using fiber optic Lloyd’s mirrors,” *Appl. Opt.* **55**, 846–852 (2016).
13. U. Rivera-Ortega, J. Dirckx, and C. Meneses-Fabian, “Fully automated low-cost setup for fringe projection profilometry,” *Appl. Opt.* **54**, 6–11 (2015).
14. H. Nguyen, D. Nguyen, Z. Wang, H. Kieu, and M. Le, “Real-time, high-accuracy 3D imaging and shape measurement,” *Appl. Opt.* **54**, 10443–10453 (2015).
15. H. Yun, B. Li, and S. Zhang, “Pixel-by-pixel absolute three-dimensional shape measurement with modified Fourier transform profilometry,” *Appl. Opt.* **56**, 1472–1480 (2017).
16. A. Briggs and O. Kolosov, *Acoustic Microscopy* (Oxford University, 2010).
17. R. G. Maev, “Advances in acoustic microscopy and high resolution ultrasonic imaging: from principles to new applications,” *Proc. SPIE* **9040**, 904007 (2014).
18. A. A. Karabutov and N. B. Podymova, “Quantitative analysis of the influence of voids and delaminations on acoustic attenuation in CFRP composites by the laser-ultrasonic spectroscopy method,” *Composites B* **56**, 238–244 (2014).
19. V. E. Gusev and A. A. Karabutov, *Laser Optoacoustics* (American Institute of Physics, 1993).
20. A. Karabutov, A. Devichensky, A. Ivochkin, M. Lyamshev, I. Pelivanov, U. Rohatgi, V. Solomatina, and M. Subudhi, “Laser ultrasonic diagnostics of residual stress,” *Ultrasonics* **48**, 631–635 (2008).

21. A. S. Bychkov, V. P. Zarubin, A. A. Karabutov, V. A. Simonova, and E. B. Cherepetskaya, "On the use of an optoacoustic and laser ultrasonic imaging system for assessing peripheral intravenous access," *Photoacoustics* **5**, 10–16 (2017).
22. V. A. Simonova, T. D. Khohlova, and A. A. Karabutov, "Wideband focused transducer array for optoacoustic tomography," *Acoust. Phys.* **55**, 888–893 (2009).
23. G. Wurzinger, R. Nuster, N. Schmitner, S. Gratt, D. Meyer, and G. Paltauf, "Simultaneous three-dimensional photoacoustic and laser-ultrasound tomography," *Biomed. Opt. Express* **4**, 1380–1389 (2013).
24. N. Wilt, *The CUDA Handbook: A Comprehensive Guide to GPU Programming* (Pearson Education, 2013).
25. P. M. Morse and K. U. Ingard, *Theoretical Acoustics* (Princeton University, 1968).
26. R. Szeliski, *Computer Vision: Algorithms and Applications* (Springer, 2010).
27. A. S. Bychkov, E. B. Cherepetskaya, A. A. Karabutov, and V. A. Makarov, "Toroidal sensor arrays for real-time photoacoustic imaging," *J. Biomed. Opt.* **22**, 076003 (2017).
28. J. Krautkrämer and H. Krautkrämer, *Ultrasonic Testing of Materials* (Springer, 2013).